RSC Advances

RSC Advances

www.rsc.org/advances

ROYAL SOCIETY OF CHEMISTRY

www.rsc.org/advances

Journal Name

ARTICLE TYPE

Carbon-doped titania nanoplates with exposed {001} facets: Facile synthesis, characterization and visible-light photocatalytic performance

Jian-Wen Shi,*[a] Chang Liu,[a] Chi He,[b] Jun Li,[a] Chong Xie,[a] Shenghui Yang,[a] Jian-Wei Chen,[c] Shi Li[d] and Chunming Niu*[a]

C-doped TiO$_2$ nanoplates (CTNP) with exposed {001} facets were successfully synthesized by hydrothermal treatment of TiC powder in a HF-HNO$_3$ mixed aqueous solution for the first time. The effects of hydrothermal temperature (140, 160, 180 and 200 ^{o}C) on the crystal phase, morphology,
10 specific surface area and porous property, surface element composition, optical response property of the resultant samples were investigated in detail, and the photocatalytic activities of these obtained CTNP samples for the degradation of methylene blue (MB) were evaluated under visible light irradiation. The results showed that precursor cubic TiC was transformed into anatase TiO$_2$ with the morphology of well-defined nanoplate completely after hydrothermal treatment 30 h. The specific surface area of CTNP was
15 significantly improved in comparison with that of micrometer sized C-doped TiO$_2$ plates (CTP) due to smaller particle size. Due to C-doping, CTNP presented red-shift absorption edge, which supported it with strong visible-light response. All these factors led to as-prepared CTNP having more excellent visible-light photocatalytic activity in comparison with micrometer sized CTP. The CTNP synthesized at 180 ^{o}C presented the optimal visible-light photocatalytic activity with a high reaction rate constant
20 (0.03692 min^{-1}) among the four CTNP samples. Based on the results of the present study, a reasonable mechanism of photocatalysis on CTNP under visible light was proposed.

1. Introduction

Owing to the various potential applications in energy and environmental field, semiconductor photocatalysis has attracted
25 considerable attention in the recent decades.[1,2] As an outstanding photocatalyst, titania (TiO$_2$) has gained much research fascination due to its excellent properties, such as environmental friendliness, chemical stability, and low cost.[3,4] However, the photocatalytic activity of TiO$_2$ is still far below the level of practical application
30 due to two main drawbacks: fast charge-carrier recombination and restrictive light absorption (only responsive to ultraviolet light with wavelength below 387 nm due to its wide band-gap).[5,6] To improve its photocatalytic activity and the possibility of practical application, many approaches have been explored.
35 Morphology control and ion doping are considered as two very promising strategies.[7,8]

Both theoretical and experimental studies have demonstrated that the photocatalytic activity of TiO$_2$ can be tuned by morphological control, especially the exposed specific crystal
40 facets.[9-11] It is widely accepted that the catalytic reactivity of anatase TiO$_2$ {001} facets is higher than that of the thermodynamically stable {101} facets due to the fact that the higher surface energy of {001} facets is more efficient for dissociative adsorption of reactant molecules in comparison with
45 that of {101} facets,[12,13] which is helpful to the reduction of charge-carrier recombination. Even more inspiringly, recent studies show crystal facets play an important role in the separation of photogenerated electron-hole pairs.[14] Owing to the

difference of energy levels of crystal facets, the photogenerated
50 electrons and holes can be separated between the different crystal facets, which can efficiently prevent their recombination to improve catalytic activity of anatase TiO$_2$.[15] In the process of exploring anatase TiO$_2$ with high reactive {001} facets, a lot of progress has been made in succession. The exposure ratio of {001}
55 facets was constantly refreshed, from 47% to 64%, 80%, 89%, 98.7, even to 100%,[9,16-20] and enhanced photocatalytic activity of anatase TiO$_2$ resulted from the exposure of high reactive {001} facets has been confirmed by many reports.[21-23] However, the photocatalytic activity of anatase TiO$_2$ with high reactive {001}
60 facets is still limited by narrow light absorption. From the viewpoint of utilizing solar light, visible light responsive TiO$_2$ crystals with high reactive {001} facets are highly desired.

It is well known that ion doping, especially nonmetal doping, is a very promising strategy for extending the photo-response of
65 TiO$_2$ from UV to visible light region.[24,25] Therefore, it may be a promising attempt to develop new TiO$_2$-based photocatalysts by incorporating the high active {001} facets and the ion doping together. In this regard, some substantial progress has been made recently. Nonmetal doped TiO$_2$ crystals (e.g. N, S, F) with
70 exposed {001} facets have been synthesized successfully by treating corresponding titanium precursor (e.g., TiN, TiS$_2$, TiOF$_2$),[26-28] and their visible-light photocatalytic activities have been demonstrated. Although TiC has been used as precursor to prepare C-doped TiO$_2$ photocatalysts, these resultant products are
75 no exposed {001} facets.[29-34] Until recently, micrometer-sized C-doped TiO$_2$ plates (CTP) with exposed {001} facets were successfully synthesized by the hydrothermal treatment of TiC in

the presence of HF.[35] Furthermore, it was demonstrated that the resulting CTP exhibited much higher photocatalytic activity than that of the C-doped TiO_2 particles due to the presence of exposed {001} facets. However, the obtained CTP existed in an aggregated form with the size of several micrometers, which inevitably resulted in its low specific surface areas (12 m^2/g),[35] and then hampered the enhancement of photocatalytic activity. Compared with micrometer-sized particles, nanoparticles possess smaller particle size and larger specific surface area. Smaller particle size is in favor of the shifting of photo-generated carriers to the surface of photocatalyst and then reacting with reactants, and samples with larger specific surface area can pre-adsorb more reactants. Both of them are helpful to avoid the recombination of photo-generated electrons and holes. Therefore, nanometer-sized C-doped TiO_2 plates with exposed {001} facets may be an ideal approach to obtain visible-light photocatalysts with higher activity. However, it has never been reported so far.

In current work, we successfully synthesized C-doped TiO_2 nanoplates (CTNP) with exposed {001} facets by hydrothermal treatment of TiC powder in a HF-HNO_3 mixed aqueous solution for the first time. TiC powder was employed as both TiO_2 precursor and carbon dopant source. HF was used as facet controlling reagent, and HNO_3 was utilized as reactant to react with TiC. For comparison, micrometer-sized CTP with exposed {001} facets were also prepared based on the previous work.[35] The crystal phase, morphology, surface element composition, optical response property, specific surface area and porous property of the resultant samples were investigated in detail, and their photocatalytic activities were evaluated by the photocatalytic decoloration of methylene blue (MB) solution under visible light irradiation ($\lambda > 420$ nm). The results showed that the photocatalytic activity of CTNP was significantly enhanced due to smaller particle size and higher specific surface area in comparison with micrometer-sized CTP. To our knowledge, this is the first time to successfully synthesize nanometer-sized C-doped TiO_2 plates with exposed {001} facets, and this is the first time to systematically evaluate the photocatalytic activity of these obtained CTNP photocatalysts.

2. Experimental

2.1 Preparation of CTNP with exposed {001} facets

Titanium carbide solid powder (TiC, particle size: ~50 nm, Aladdin Reagent Company) was employed as TiO_2 precursor. In a typical synthesis route, 3.0 mL of HNO_3 (68%) and 20.0 mL of ultrapure water were mixed under vigorous stirring to form solution. Then, 0.9 g of TiC powder was added into the solution. After stirring for 30 min, 3.0 mL of HF (40%) was added. After continuously stirring for an hour, the suspension was transferred to a 50 mL Teflon-lined autoclave and heated at a given temperature (such as 140, 160, 180 and 200 °C) for 30 hours. After the hydrothermal process, the products were collected by centrifugation and washed with ultrapure water for several times, and then were dried overnight at 80 °C in air. For convenience, the samples were marked according to the different hydrothermal temperature as S-140, S-160, S-180 and S-200, respectively.

2.2 Preparation of CTP with exposed {001} facets

The preparation of CTP with exposed {001} facets was based on the previous work.[35] TiC powder (particle size: 2~4 μm, Aladdin Reagent Company) was employed as the TiO_2 precursor. In a typical synthesis route, 0.9 g of TiC powder was mixed with 30 mL of the mixed aqueous solution of HF (1.86 M) and HNO_3 (4.96 M) under vigorous stirring to form solution. After stirring

for an hour, the suspension was transferred to an 80 mL Teflon-lined autoclave and heated at 180 °C for 30 hours. After the reaction, the products were collected by centrifugation and washed with ultrapure water for several times, and then were dried overnight at 80 °C in air.

2.3 Characterizations

X-ray diffraction (XRD) patterns were recorded at room temperature with a Rint-2000 Rigaku diffractometer with copper K_{a1} radiation. Scanning electron microscopy (SEM) images were obtained by FEI Quanta 250 equipment. Transmission electron microscope (TEM) and the selected-area electron diffraction (SAED) pattern were carried out on JEM-2100 HT. The nitrogen adsorption measurements were taken at 77 K using an Autosorb-iQ analyzer (Quantachrome, America), and the Barrett–Joyner–Halenda (BJH) pore diameter distribution curves were obtained from the desorption branch and specific surface areas were obtained according to the Brunauer–Emmett–Teller (BET) model. X-ray photoelectron spectroscopy (XPS) analyses were tested on an Escalab 250 (Thermo Scientific, America) with aluminum K_a radiation. UV-Vis absorption spectroscopies were recorded by a V-670 spectrophotometer (Jasco, Japan) equipped with an integrating sphere, and the baseline correction was done using a calibrated sample of barium sulfate.

2.4 Experimental procedures of photocatalytic decoloration

The photocatalytic experiment was carried out in a photo reaction system (as illustrated in our previous publication[36]) by using MB as a model pollutant. A 1000 W Xe lamp equipped with a 420 nm glass filter (removing the UV irradiation below 420 nm), positioned in the center of a water-cooled quartz jacket, was used to offer visible light irradiation. At the side of quartz jacket, a 50-mL cylindrical vessel was used as the reactive bottle to load reaction solution. The distance between lamp and reactive bottle was 40 mm. In the bottom of the reactive bottle, a magnetic stirrer was equipped to achieve effective dispersion. The temperature of the reaction solution was maintained at 30 ± 0.5 °C by cooling water. Photocatalyst powder (50 mg) was added into 50 mL of 3×10^{-5} M MB solution to form suspension. Then, the suspension was irradiated with visible light. During the irradiation, the suspension was stirred continuously. At given time interval, 3 mL of suspension was taken out and immediately centrifuged to eliminate solid particles. The absorbance of filtrate was measured by a spectrophotometer at the maximum absorbance peak 665 nm.

### 2.5 The measurements of hydroxyl radicals (•OH)

Photocatalyst powder (50 mg) was suspended in 50 mL aqueous solution containing 0.01 M of NaOH and 3 mM of terephthalic acid. Before exposure to visible light irradiation ($\lambda > 420$ nm), the suspension was stirred in dark for 30 min. Then 3 mL of the solution was taken out after every 30 min, and centrifuged for fluorescence spectrum measurements. During the photoreactions, no oxygen was bubbled into suspension. A fluorescence spectrophotometer (Hitachi, F-4600) was used to measure the fluorescence signal of the 2-hydroxy terephthalic acid generated. The excitation light employed in recording fluorescence spectra was 313 nm.

3. Results and discussion

3.1 Crystal phase structure

XRD analysis was carried out to explore the crystal phase of all samples. The five peaks appear in the XRD pattern of TiC (Fig. 1) at 2θ = 36.04°, 41.99°, 60.55°, 72.10° and 76.16°, which are corresponding to (111), (200), (220), (311) and (222) planes of

[5] cubic TiC, respectively (Ref. No 00-005-0693). The peaks at 2θ = 25.28°, 37.80°, 48.05°, 53.89°, 55.06°, 62.69°, which all belong to anatase TiO_2 (Ref. No 00-021-1272), appear in the XRD patterns of four CTNP samples and CTP sample, and no peak assigned to cubic TiC can be observed, implying the structure of cubic TiC

[10] has collapsed completely to form the structure of anatase TiO_2 after hydrothermal treatment for 30 h, and temperature changes in the range of 140 to 200 °C have not obviously affected crystal phase transition from cubic TiC to anatase TiO_2. A new and minor peak at 2θ = 23.40° appears in the XRD patterns of four

[15] CTNP samples and CTP sample, which is corresponding to (100) plane of cubic titanium oxide fluoride ($TiOF_2$) (Ref. No 01-077-0132), indicating there are trace amounts of $TiOF_2$ in the structure of anatase TiO_2. By carefully examining, a weak peak can be observed at about 2θ = 27.4° in the XRD patterns of S-180 and S-

[20] 200, which can be attributed to the diffraction of (110) crystal planes of rutile TiO_2 (Ref. No 01-078-1508), indicating that anatase TiO_2 can be transformed into rutile TiO_2 in our experimental conditions when hydrothermal treatment is carried out at higher temperature (above 180 °C). The crystal

[25] composition of all samples is listed in Table 1.
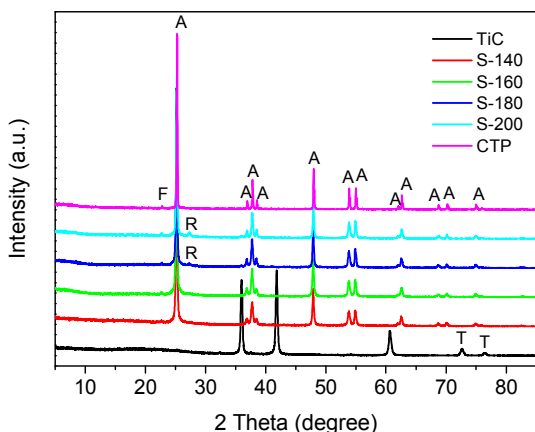
Fig. 1 The XRD patterns of all samples (A: anatase; R: Rutile; F: $TiOF_2$; T: TiC).

[30] **Table 1** The crystal composition and S_{BET} of samples

| Sample	TiC (%)	Anatase (%)	Rutile (%)	$TiOF_2$ (%)	S_{BET} ($m^2 g^{-1}$)
TiC	100	0	0	0	44.42
S-140	0	100	0	TA*	67.36
S-160	0	100	0	TA	56.79
S-180	0	99	1	TA	42.16
S-200	0	97	3	TA	40.90
CTP	0	100	0	TA	8.68

*trace amount (TA)

It is well known that TiO_2 has three different crystal phases, brookite, anatase and rutile. Among these, anatase and rutile are the most studied phases, and anatase is generally considered to be

[35] the active component based on the comparison between anatase and rutile. It is widely accepted that TiO_2 consisted of the mixed phases of anatase and rutile with an appropriated ratio has higher photocatalytic activity than single phase, and Degussa P25 is the outstanding representative of this photocatalyst. As confirmed by

[40] XRD, both S-180 and S-200 are composed of the mixed phases of major anatase TiO_2 and a little of rutile TiO_2. This mixed phase has positive contribution to their photocatalytic performances.

3.2 Morphology

The morphologies of all samples are displayed in Fig. 2. As

[45] shown in Fig. 2a, TiC particles present irregular morphology with the size of about 50 nm. S-140 consists of a large number of particles with uniform size of about 65 nm, and some plate-shaped particles with square outline (side length: ~60 nm) can be observed (Fig. 2b). Compared with S-140, these particles grow up

[50] a little in S-160 sample (Fig. 2c), with the side length of about 70 nm. When the hydrothermal temperature was ascended to 180 °C, many TiO_2 plates with a square outline formed (Fig. 2d), and the two flat and square surfaces can be ascribed to {001} and the eight isosceles trapezoidal surfaces are {101} facets of

[55] anatase TiO_2 crystal,[9] as illustrated in the inset in Fig. 2d. The side length and the thickness of TiO_2 plates are about 160 nm and 25 nm, respectively. The percentage of {001} facets is estimated to be ca. 70%. However, the product size in S-180 is not so uniform because some plates with smaller size (side length: ~90

[60] nm, ~50 nm), and even some particles with irregular morphology can be observed. Compared with S-180, the morphology of S-200 has not obvious change (Fig. 2e), and the product size is not uniform, either. As a comparison, the SEM image of the CTP sample is presented in Fig. 2f. The side length and the thickness

[65] of TiO_2 plates are about 3.4 μm and 500 nm, respectively, and the percentage of {001} facet is estimated to be ca. 76%. It should be noted that these plates intercross each other without obvious regularity to form large blocks, which is not conducive to the enhancement of the specific surface area of sample, and is also

[70] harmful to the exposure of {001} facets to inter-medium.
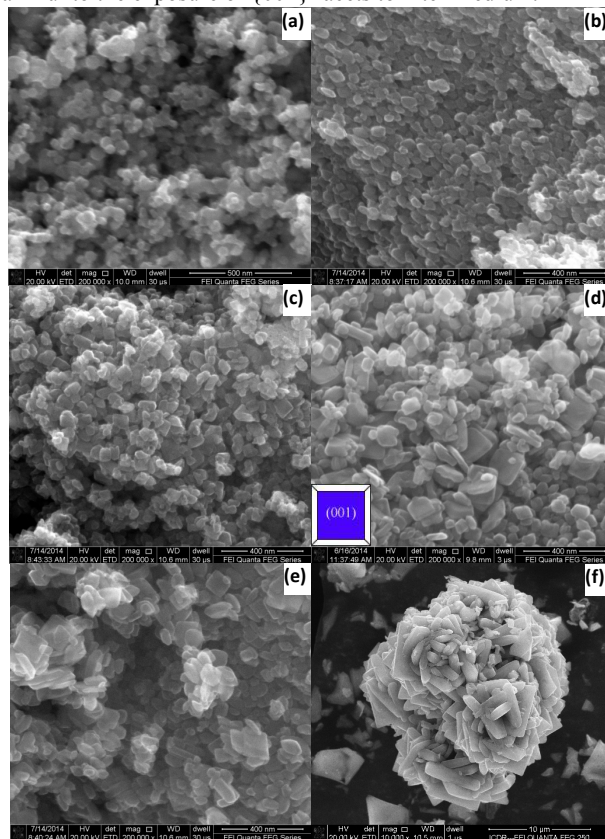
Fig. 2 SEM images of all samples: (a) TiC; (b) S-140; (c) S-160; (d) S-180; (e) S-200; (f) CTP.

Fig. 3 displays the TEM images with different magnification of S-180 sample. The low magnified TEM images clearly demonstrate that TiO_2 plates with a square outline have formed (Figs. 3a and 3b), which is in good agreement with the SEM results. The HR-TEM image recorded from the white circled area in Fig. 3b clearly displays the continuous (200) atomic planes with a lattice spacing of 0.19 nm (Fig. 2c), corresponding to the {200} planes of anatase TiO_2,[16] which confirms the exposed crystal facet is the {001} facet. The selected-area electron diffraction (SAED) pattern (Fig. 2d) displays the diffraction spots, confirming that the as-prepared TiO_2 plate is a single crystal.
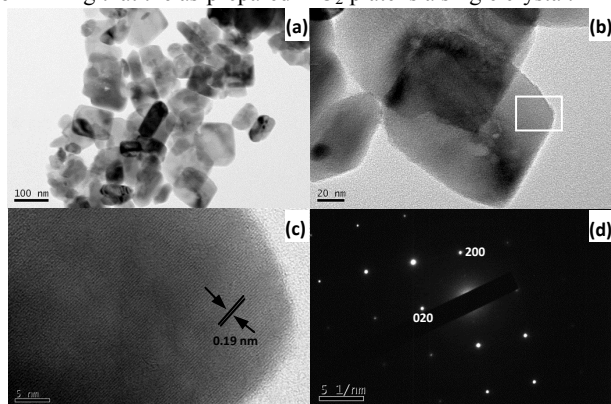
Fig. 3 TEM image with different magnification (a) and (b), the high-resolution TEM image (c) and SAED pattern (d) of S-180.

### 3.3 Specific surface area and porous property

In order to gain the information about specific surface area and porous property, nitrogen adsorption–desorption experiments were carried out. It can be seen that from Fig. 4 the four CTNP samples are similar and present hysteresis loops, which can be classified as type IV according to IUPAC classification,[37] indicating the presence of mesopores. These isotherms exhibit H3 hysteresis loops associated with the presence of slit-like pores, which can be attributed the pores formed from the stack of plates. In comparison, the hysteresis loop of CTP sample has a smaller area and the adsorbed volume of CTP sample has a smaller value, implying there are fewer pores in the structure of CTP sample, which results in its lower specific surface area. The pore-size distributions (inset in Fig. 4) demonstrate the existence of mesopores in all samples. S-140 and S-160 share a similar pore-size distribution property, and S-180 and S-200 share another similar pore-size distribution property. Pore size regions of S-140 and S-160 are mainly mesopore with two sharp maximums at about 3.7 nm and 15.5 nm. Compared with S-140 and S-160, mesopores with size between 1.7 nm and 5 nm have decreased in S-180 and S-200 samples, and the peak maximum has been shifted to about 34 nm from 15.5 nm, which can be attributed the growth of particles, as proved in SEM analysis. The specific surface areas of TiC, S-140, S-160, S-180, S-200 and CTP are 44.42, 67.36, 56.79, 42.16, 40.90 and 8.68 m^2 g^{-1} based on the BET analysis, indicating that the specific surface area of obtained sample is inversely proportional to the hydrothermal temperature. In addition, the specific surface area of CTNP is significantly improved in comparison with that of micrometer sized CTP. The higher surface area can provide the possibility for the efficient pre-adsorption, diffusion and transportation of the degradable organic molecules and hydroxyl radicals in photocatalytic reaction, which will lead to the enhanced photocatalytic activity.
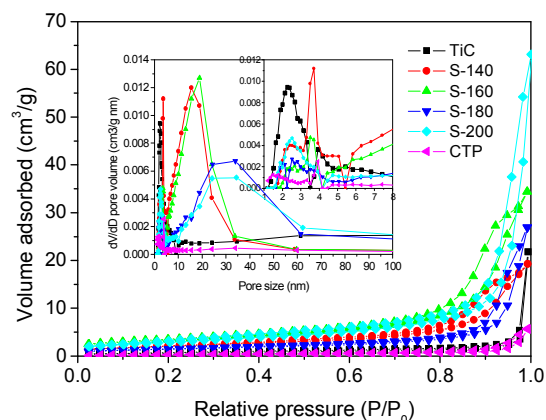
Fig. 4. Nitrogen adsorption and desorption isotherms and pore diameter distribution curves of samples

3.4 Surface element composition

Figs. 5a and 5b display the deconvoluted XPS spectra of Ti2p and C1s for S-180, respectively, along with its precursor TiC. As reported in early papers,[31,32,35,38] the peaks observed for the precursor TiC include 455.1 eV (Ti 2p5/2) and 461.1 eV (Ti 2p3/2) (Fig. 5a), which can be attributed to Ti-C, and the peak at 459.0 eV can be assigned to Ti-O in TiO_2, which resulted from the oxidization of a very small fraction TiC on its surface. In contrast, the peaks assigned to TiC phase are disappear and a new peak at 464.7 eV, which can be assigned to Ti 2p1/2 of TiO_2, appears for S-180, confirming TiC phase has been transformed into anatase TiO_2, which is consistent with XRD analysis. The peak at 281.8 eV (Fig. 5b) is characteristic of TiC, which originates from Ti-C linkage.[31,38] The peak at 282.9 eV is denoted as C-Ti* in early publications,[39,40] which is partly a feature of the nanocomposite, and is partly due to sputter damage. The peak at 284.7 eV is generally attributed to elemental carbon,[41-44] which is the strongest peak among all fitted C1s peaks, implying there are a large number of elemental carbons on the surface of sample. These elemental carbons can be attributed to unformed carbons during the transformation of TiC to C-doped TiO_2 due to low reaction temperature. As confirmed by early publications,[45-47] these unformed carbons can act as photosensitizer to promote visible light response. Both the two peaks (281.8 and 282.9 eV) corresponding to TiC are disappear in the XPS spectrum of C1s for S-180, which further proves TiC phase was transformed into anatase TiO_2. The peaks at 285.9 and 286.2 eV are usually assigned to C–O-like species.[32,48] The new weak peak appeared at about 289.3 eV can be assigned to -C=O bond, which can also be attributed to the formation of C–O bonds due to the replacement of Ti atom by C atom in the lattice of TiO_2 that form the Ti-O-C structure.[31,32,35,49,50] The percentage of carbon existing as Ti-O-C in total carbon for S-180 can be calculated by the integral of the areas below the four peaks, and the result is 8.58 %. Based on the above observations, it is confirmed that self-doping of carbon occurs during the hydrothermal treatment of TiC powder.
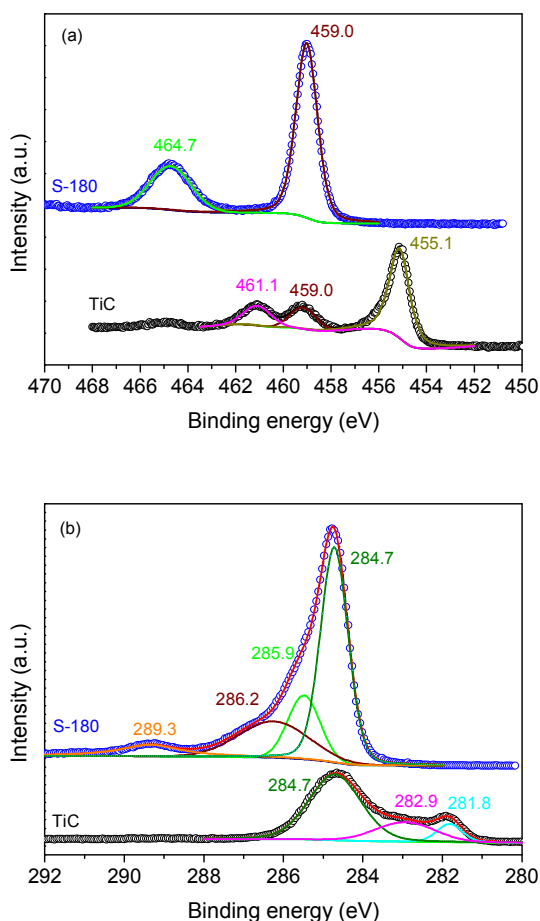
Fig. 5. Deconvoluted XPS spectra of Ti2p (a) and C1s (b) regions for TiC and S-180.

3.5 Optical response property

Fig. 6 shows the optical response property of all samples by UV–Vis absorption spectroscopy, together with Degussa P25 as comparison. TiC powder, with the color of black, exhibits strong absorption in whole range of wavelength employed (200~800 nm). Due to the formation of anatase, as confirmed by XRD analysis, the characteristic absorption edge at around 350~390 nm of semiconductor TiO_2 can be clearly observed from the spectra of other five samples (S-140, S-160, S-180, S-200 and CTP), and their characteristic absorption edges are more obvious with the enhancement of hydrothermal temperature (S-140 and S-160 present a lower absorption transition in comparison with S-180, S-200 and CTP). Furthermore, the five samples (S-140, S-160, S-180, S-200 and CTP) present red-shift absorption edge in comparison with P25. The band gaps estimated by the Kubelka-Munk method are 3.10, 2.04, 2.19, 2.93, 3.06 and 3.00 eV for P25, S-140, S-160, S-180, S-200 and CTP, respectively.[51,52] The reason of red-shift absorption edge may be attributed to the appearance of some localized states in the band gap of TiO_2 due to C-doping, which are directly responsible for the narrowing of band gap, allowing visible light absorption.[53,54] The band gaps of S-140 and S-160 presents significant decrease in comparison with that of P25, S-180, S-200 and CTP, which can be induced by unformed C (as confirmed by XPS, elemental carbon) remained

on the surface of obtained samples. The unformed C can lead to the strong absorbance in visible region, as illustrated in Fig. 6. In addition, the absorption in the visible region decreases with the enhancement of hydrothermal temperature, which can be attributed the escape of unformed C from their structures in the process of hydrothermal treatment.
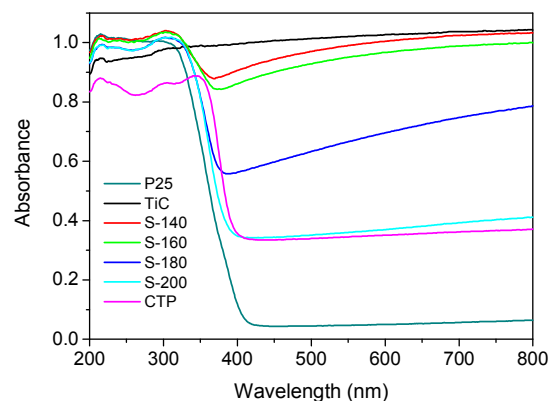

**Fig. 6** UV–vis absorption spectra of samples.

3.6 Photocatalytic activity

The photocatalytic activities of all samples were evaluated by the decoloration of MB solution without investigating the degradation intermediates in detail. Before photocatalysis, the solution including MB and catalyst was stirred in dark for one hour for establishing the adsorption equilibrium. The decoloration of MB solution versus photocatalytic time under visible light irradiation ($\lambda > 420$ nm) is shown in Fig. 7. After stirring in the dark for 60 min, the concentration of MB reduced slightly (1.5 %) with adding of CTP, indicating the adsorption ability of CTP is weak due to low specific surface area resulted from micrometer size. In comparison, other samples, including CTNP and TiC, show some adsorption ability mainly due to higher specific surface area resulted from nano-meter scale. Due to the fact that TiC has not photocatalytic activity, MB molecules are hardly decomposed in the presence of TiC as photocatalyst. CTP except TiC presents the worst photocatalytic activity due to large particle size, low specific surface area. Owing to smaller particle size and higher specific surface area, the photocatalytic activity of CTNP is enhanced in comparison with micrometer-sized CTP. The photocatalytic activities of all samples increase in the order TiC < CTP < S-140 < S-160 < S-200 < S-180. S-180 displays optimal visible-light photocatalytic activity among all samples, and MB solution can be completely decolorized in 120 min.
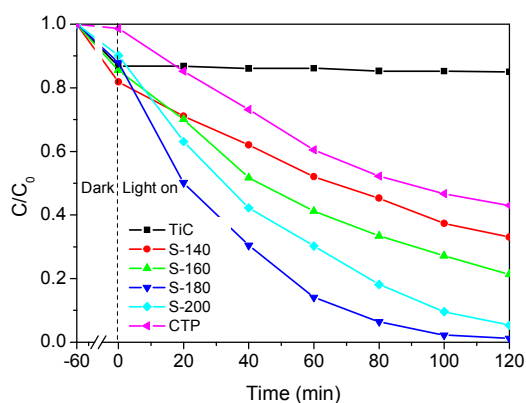
Fig. 7. Photocatalytic decoloration of MB solution over different photocatalysts under visible light irradiation.

5

To understand the reaction mechnism of MB degradation, we applied the pseudo-first order model as expressed by the equation $ln(C_0/C) = kt$ (where C_0 and C are the concentrations of MB in solution at time 0 and t, respectively, and t is the reaction time; k
10 is the reaction rate constant (min^{-1})), which is generally used for photocatalytic degradation process,[55,56] to treat the experimental data. The $ln(C_0/C)$s are plotted against t for reactions using TiC, S-140, S-160, S-180, S-200 and CTP as the photocatalyst, respectively. The straight line fitting indicates that the reaction
15 kinetics is first order indeed for all samples (Fig. 8). The reaction rate constants deduced from the slopes are 0.00019, 0.00792, 0.01160, 0.03692, 0.02342 and 0.00720 min^{-1} for TiC, S-140, S-160, S-180, S-200 and CTP, respectively. The rate constants corresponding to the visible light photocatalytic activity are
20 enhanced to 5.13 times from CTP to S-180 due to the facts that the plate size is reduced from micron of CTP (3.4 μm in side length and 500 nm in thickness) into nanometer of S-180 (160 nm in side length and 25 nm in thickness) and the specific surface area is enhanced from 8.68 m^2 g^{-1} of CTP into 42.16 m^2 g^{-1} of S-
25 180. Among the four CTNP samples, S-180 presents optimal visible-light photocatalytic activity with a high reaction rate constant (0.03692 min^{-1}), which is much higher than previously reported values for TiO_2-based photocatalysts (e.g. TiO_2 nanotube films (0.0019 min^{-1}),[57] N-doped TiO_2 particles (0.00333
30 min^{-1}),[58,59] carbon-covered TiO_2 (0.0091 min^{-1}),[60] WO_3-TiO_2 nano porous semiconductors (0.0129 min^{-1}),[61] chromium (III) doped mesoporous TiO_2 (0.0158 min^{-1})[62]) and other new photocatalysts ($CdBiYO_4$ (0.0137 min^{-1}),[59] $BiVO_4$ (0.00252 min^{-1})[63], etc).
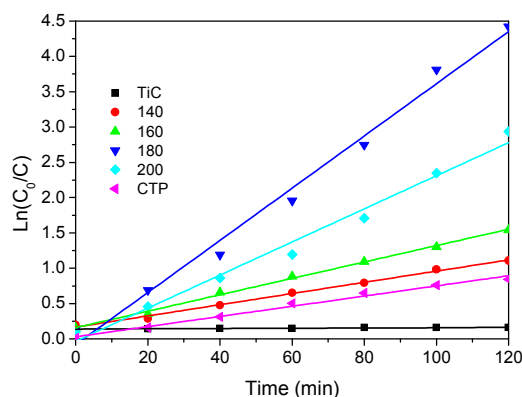

35

3.7 Photocatalytic stability

The stability of catalyst is an important property, which
40 directly relates to the life time of the catalyst. A cycle experiment on photocatalytic decomposing of MB by S-180 was designed to examine the stability of as-prepared NTP/CdS. As shown in Fig. 9. S-180 maintains its photocatalytic activity for MB decoloration after six cycles without observable change. Therefore, it can be
45 deduced that S-180 is a stable photocatalyst.
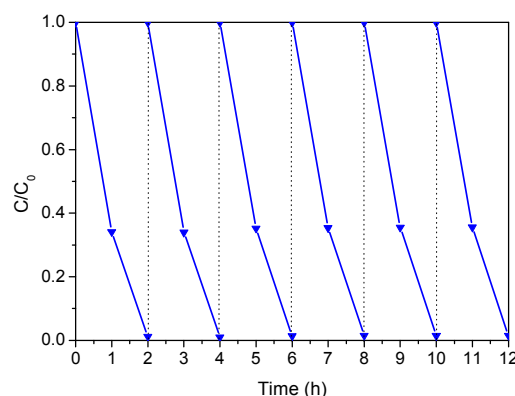
Fig. 9. Cycling test results of photocatalytic activity (MB decoloration) of S-180 under visible light irradiation.

3.8 The amount of hydroxyl radicals

50 Hydroxyl radical (•OH) is a very important species produced in the process of photocatalysis, which is responsible for the decomposition of organic pollutant. The •OH radicals are mainly generated from the oxidative reaction between photo-induced holes and H_2O or OH^-, and the reductive reaction between photo-
55 induced electrons and O_2. So that the amount of •OH radicals produced corresponds to the separation efficiencies of photo-induced electrons and holes as well as the photocatalytic activity.[64-66] Moreover, the experiment of measuring active •OH can avoid the dye self-photosensitization effect and prove
60 photocatalytic activity under visible light. As displayed in Fig. 10a, a gradual increase of the fluorescence intensity is observed when S-180 was used as photocatalyst, implying that the fluorescence was excited by 2-hydroxyterephthalic acid coming from the photocatalytic reaction. The comparison of the
65 fluorescence intensities of S-180 and CTP under visible light irradiation in 120 min is showed in Fig. 10b. Compared with CTP, S-180 produced more •OH radicals, indicating S-180 possesses higher separation efficiency of photo-generated electrons and holes as well as higher photocatalytic activity, which can be
70 attributed to the fact that S-180 can effectively decrease the recombination of photo-generated electrons and holes due to its smaller particle size. In addition, the nearly linear relationship between fluorescence intensity and irradiation time confirms the stability of S-180 as photocatalyst.
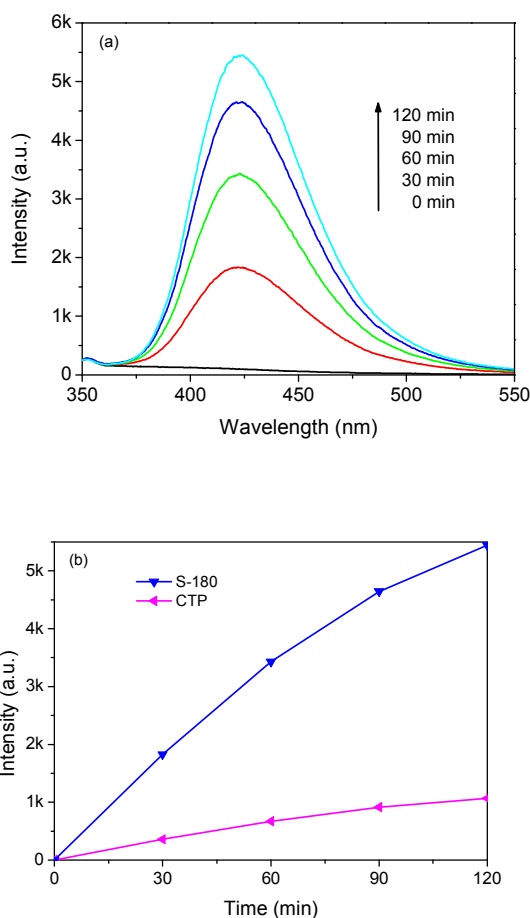
Fig. 10. (a) Fluorescence spectra of S-180 in 3 mM terephthalic acid irradiated by visible light at different irradiation time; (b) Comparison of the fluorescence signal intensities at 423 nm of S-180 and CTP.

3.9 Proposed mechanism

Fig. 11 schematically depicts the band structure, electron-hole pairs generation and separation, and catalytic reaction mechanism for the decoloration of MB on CTNP under visible light irradiation. Firstly, due to the photosensitization, unformed C can absorb visible light to produce electrons and inject electrons into the conduction band (CB) of TiO_2. Secondly, due to carbon doping, the electrons in the localized carbon states can be excited to the conduction band under visible light irradiation. Then these electrons will be scavenged by by molecular oxygen to produce the superoxide radical anion $\bullet O_2^-$ and hydrogen peroxide H_2O_2. These new formed intermediates can inter-react to produce hydroxyl radicals ($\bullet$OH). In addition, the photo-generated holes formed in the localized C states react with hydroxyl groups and H_2O molecule to produce hydroxyl radicals. Finally, dye molecules are oxidized by these oxidants and are mineralized into final products step by step.[67-69]
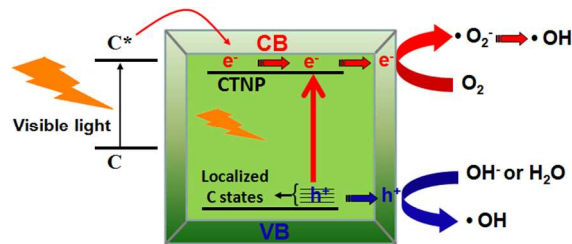
Fig. 11. Schematic illustration of band structure, electron-hole pairs generation and separation, and photocatalytic reaction mechnism.

4. Conclusions

Nanometer-sized C-doped TiO_2 plates with exposed {001} facets were successfully synthesized by hydrothermal treatment of TiC powder in a HF-HNO_3 mixed aqueous solution for the first time. The effects of hydrothermal temperature (140, 160, 180 and 200 ^{o}C) on the crystal phase, morphology, specific surface area and porous property, surface element composition, optical response property of the resultant samples were investigated in detail. Several important facts were disclosed firstly:

1) XRD revealed that precursor cubic TiC can be transformed into anatase TiO_2 completely after hydrothermal treatment 30 h at experimental temperatures. SEM demonstrated that TiO_2 nanoplates with exposed {001} facets formed, and the size of nanoplates increased with the enhancement of hydrothermal temperature. TEM further demonstrated the exposed crystal facet of TiO_2 nanoplates was the {001} facet. BET analysis disclosed that the specific surface area of CTNP was significantly improved in comparison with that of micrometer sized CTP, and the specific surface area decreased with the enhancement of hydrothermal temperature. XPS analysis demonstrated that self-doping of carbon occurred during the hydrothermal treatment of TiC powder. UV-Vis absorption showed that CTNP presented red-shift absorption edge and exhibited strong absorption in the visible region.

2) Compared with micrometer-sized CTP, the obtained CTNP presented more excellent visible-light photocatalytic activity for the decoloration of MB, which could be attributed to the crucial factors: smaller particle size and higher specific surface area of CTNP. S-180 presented optimal visible-light photocatalytic activity with a high reaction rate constant (0.03692 min^{-1}) among the four CTNP samples, which was much higher than some previously reported results.

Acknowledgements

valuable comments of anonymous reviewers are greatly appreciated.

Notes and references

[a] *Center of Nanomaterials for Renewable Energy, State Key Laboratory of Electrical Insulation and Power Equipment, School of Electrical Engineering, Xi'an Jiaotong University, Xi'an 710049, China. Fax/Tel: +86 29 83395372; E-mail:shijnwn@163.com; cniu@mail.xjtu.edu.cn.*
[b] *Department of Environmental Science and Engineering, School of Energy and Power Engineering, Xi'an Jiaotong University, Xi'an 710049, China.*
[c] *Institute of Urban Environment, Chinese Academy of Sciences, Xiamen, Fujian, 361021, China.*
[d] *Department of Environmental Science and Engineering, China University of Petroleum, Qingdao 266580, China*

1   M. R. Hoffmann, S. T. Martin, W. Choi and D. W. Bahnemannt, *Chem. Rev.*, 1995, **95**, 69.
2   U. Diebold, *Surf. Sci. Rep.*, 2003, **48**, 53.
3   A. Fujishima, X. Zhang and D. A. Tryk, *Surf. Sci. Rep.*, 2008, **63**, 515.
4   M. D. Hernandez-Alonso, F. Fresno, S. Suarez and J. M. Coronado, *Energy Environ. Sci.*, 2009, **2**, 12313.
5   X. Chen and S. S. Mao, *Chem. Rev.*, 2007, **107**, 2891.
6   L. Gomathi Devi and R. Kavitha, *Appl. Catal. B* 2013, **140–141**, 559.
7   G. Liu, L. Wang, H. G. Yang, H.-M. Cheng and G. Q. Lu, *J. Mater. Chem.*, 2010, **20**, 831.
8   J. Tian, Z. Zhao, A. Kumar, R. I. Boughtonc and H. Liu, *Chem. Soc. Rev.*, 2014, **43**, 6920.
9   H. G. Yang, C. H. Sun, S. Z. Qiao, J. Zou, G. Liu, S. C. Smith, H. M. Cheng and G. Q. Lu, *Nature*, 2008, **53**, 638.
10 D. Zhang, G. Li, X. Yang and J. C. Yu, *Chem. Commun.*, 2009, **45**, 4381.
11 S. Liu, J. Yu and M. Jaroniec, *Chem. Mater.*, 2011, **23**, 4085.
12 L. Ye, J. Mao, J. Liu, Z. Jiang, T. Peng and L. Zan, *J. Mater. Chem. A*, 2013, **1**, 10532.
13 J. Yu, L. Qi and M. Jaroniec, *J. Phys. Chem. C*, 2010, **114**, 13118.
14 R. Li, F. Zhang, D. Wang, J. Yang, M. Li, J. Zhu, X. Zhou, H. Han and C. Li, *Nat. Commun.*, 2013, **4**, 1432.
15 C. Liu, X. Han, S. Xie, Q. Kuang, X. Wang, M. Jin, Z. Xie, and L. Zheng, *Chem. Asian J.*, 2013, **8**, 282.
16 H. G. Yang, G. Liu, S. Z. Qiao, C. H. Sun, Y. G. Jin, S. C. Smith, J. Zou, H. M. Cheng and G. Q. Lu, *J. Am. Chem. Soc.*, 2009, **131**, 4078.
17 D. Zhang, G. Li, X. Yang and J. C. Yu, *Chem. Commun.*, 2009, **29**, 4381.
18 X. Han, Q. Kuang, M. Jin, Z. Xie and L. Zheng, *J. Am. Chem. Soc.*, 2009, **131**, 3152.
19 C. Wen, J. Zhou, H. Jiang, Q. Hu, S. Qiao and H. Yang, *Chem. Commun.*, 2011, **47**, 4400.
20 J. Chen, Y. Tan, C. Li, Y. Cheah, D. Luan, S. Madhavi, F. Boey, L. Archer and X. Lou, *J. Am. Chem. Soc.*, 2010, **132**, 6124.
21 M. Liu, L. Piao, L. Zhao, S. Ju, Z. Yan, T. He, C. Zhou and W. Wang, *Chem. Commun.*, 2010, **46**, 1664.
22 X. Han, Q. Kuang, M. Jin, Z. Xie and L. Zheng, *J. Am. Chem. Soc.*, 2009, **131**, 3152.
23 D. Zhang, G. Li, X. Yang and J. C. Yu, *Chem. Commun.*, 2009, **45**, 4381.
24 R. Asahi, T. Morikawa, T. Ohwaki, K. Aoki and Y. Taga, *Science*, 2001, **293**, 269.
25 S. U. M. Khan, M. Al-Shahry and W. B. Ingler Jr, *Science*, 2002, **297**, 2243.
26 G. Liu, H. G. Yang, X. Wang, L. Cheng, J. Pan, G. Q. Lu and H.-M. Cheng, *J. Am. Chem. Soc.*, 2009, **131**, 12868.
27 G. Liu, C. Sun, S. C. Smith, L. Wang, G. Q. M. Lu and H. M. Cheng, *J. Colloid Interface Sci.*, 2010, **349**, 477.
28 X. Zong, Z. Xing, H. Yu, Z. Chen, F. Tang, J. Zou, G. Q. Lu and L. Wang, *Chem. Commun.*, 2011, **47**, 11742.
29 M. Shen, Z. Wu, H. Huang, Y. Du, Z. Zou and P. Yang, *Mater. Lett.*, 2006, **60**, 693.
30 X. Cui, H. Gu, J. Lu, J. Shen and Z. Zhang, *J. Nanosci. Nanotechno.*, 2007, **7**, 3140.
31 D. E. Gu, Y. Lu, B. C. Yang and Y. D. Hu, *Chem. Commun.*, 2008, **44**, 2453.
32 V. Kiran and S. Sampath, *ACS Appl. Mater. Interfaces*, 2012, **4**, 3818.
33 V. Kiran and S. Sampath, *Nanoscale*, 2013, **5**, 10646.
34 D.-L. Shieh, S.-J. Huang, Y.-C. Lin, Y.-S. Lin, J.-L. Lin, T.-F. Yeh and H. Teng, *Micropor. Mesopor. Mat.*, 2013, **167**, 237.
35 J. Yu, G. Dai, Q. Xiang and M. Jaroniec, *J. Mater. Chem.*, 2011, **21**, 1049.
36 J.-W. Shi, X. Zong, X. Wu, H.-J. Cui, B. Xu, L. Wang and M.-L. Fu, *ChemCatChem*, 2012, **4**, 488.
37 Michal Kruk and Mietek Jaroniec, *Chem. Mater.*, 2001, **13**, 3169.
38 V. Kiran, S. B. Kalidindi, B. R. Jagirdar, S. Sampath, *Electrochim. Acta*, 2011, **56**, 10493.
39 E. Lewin, P.O.Å. Persson, M. Lattemann, M. Stüber, M. Gorgoi, A. Sandell, C. Ziebert, F. Schäfers, W. Braun, J. Halbritter, S. Ulrich, W. Eberhardt, L. Hultman, H. Siegbahn, S. Svensson and U. Jansson, *Surf. Coat. Tech.*, 2008, **202**, 3563.
40 M. Magnuson, E. Lewin, L. Hultman and U. Jansson, *Phys. Rev. B*, 2009, **80**, 235108.
41 F. Dong, H. Wang and Z. Wu, *J. Phys. Chem. C*, 2009, **113**, 16717.
42 J. A. Rengifo-Herrera, J. Kiwi and C. Pulgarin, *J. Photochem. Photobiol. A*, 2009, **205**, 109.
43 L. Zhao, X. Chen, X. Wang, Y. Zhang, W. Wei, Y. Sun, M. Antonietti and M.-M. Titirici, *Adv. Mater.*, 2010, **22**, 3317.
44 X. Yang, C. Cao, K. Hohn, L. Erickson, R. Maghirang, D. Hamal and K. Klabunde, *J. Catal.*, 2007, **252**, 296.
45 F. Dong, H. Wang, Z. Wu, *J. Phys. Chem. C*, 2009, **113**, 16717.
46 L. Zhao, X. Chen, X. Wang, Y. Zhang, W. Wei, Y. Sun, M. Antonietti, M.-M. Titirici, *Adv. Mater.*, 2010, **22**, 3317.
47 X. Yang, C. Cao, K. Hohn, L. Erickson, R. Maghirang, D. Hamal, K. Klabunde, *J. Catal.*, 2007, **252**, 296.
48 Y. Cong, X. Li, Y. Qin, Z. Dong, G. Yuan, Z. Cui and X. Lai, *Appl. Catal. B*, 2011, **107**, 128.
49 V. Kiran, S. B. Kalidindi, B. R. Jagirdar and S. Sampath, *Electrochim. Acta*, 2011, **56**, 10493.
50 H. Q. Wang, Z. B. Wu and Y. Liu, *J. Phys. Chem. C*, 2009, **113**, 13317.
51 L. Wan, J. F. Li, J. Y. Feng, W. Sunb and Z. Q. Mao, *Mater. Sci. Eng., B*, 2007, **139**, 216.
52 J. Zhang, J. Xi and Z. Ji, *J. Mater. Chem.*, 2012, **22**, 17700.
53 C. Di Valentin, G. Pacchioni and A. Selloni, *Chem. Mater.* 2005, **17**, 6656.
54 X. Chen and C. Burda, *J. Am. Chem. Soc.* 2008, **130**, 5018.
55 S. Liu, J. Yu and M. Jaroniec, *J. Am. Chem. Soc.*, 2010, **132**, 11914.
56 S. Han, L. Hu, N. Gao, A. A. Al-Ghamdi and X. Fang, *Adv. Funct. Mater.*, 2014, **24**, 3725.
57 W.-Y. Wang and B.-R. Chen, *Int. J. Photoenergy*, 2013, 348171.
58 J. Luan and Z. Hu, *Int. J. Photoenergy*, 2012, 301954.
59 H. Du and J. Luan, *Solid State Sci.*, 2012, **14**, 1295.
60 L. Lin, W. Lin, Y. X. Zhu, B. Y. Zhao, Y. C. Xie, Y. He and Y. F. Zhu, *J. Mol. Catal. A*, 2005, **236**, 46.
61 M. R. Bayati, F. Golestani-Fard, A. Z. Moshfegh and R. Molaei, *Mater. Chem. Phys.*, 2011, **128**, 427.
62 K. B. Jaimy, S. Ghosh, S. Sankar and K. G. K. Warrier, *Mater. Res. Bull.*, 2011, **46**, 914.
63 J. Zhang, H. Cui, B. Wang, C. Li, J. Zhai and Q. Li, *Chem. Eng. J.*, 2013, **223**, 737.
64 T. Hirakawa and Y. Nosaka, *Langmuir*, 2002, **18**, 3247.
65 J. Zhang, W. Fu, J. Xi, H. He, S. Zhao, H. Lu and Z. Ji, *J. Alloys Compd.*, 2013, **575**, 40.
66 J. Zhang, L. Qian, W. Fu, J. Xi, and Z Ji, *J. Am. Ceram. Soc.*, 2014, **97**, 2615.
67 F.B. Li, X.Z. Li, M.F. Hou, K.W. Cheah and W.C.H. Choy, *Appl. Catal. A*, 2005, **285**, 181.
68 J.-W. Shi, X. Yan, H.-J. Cui, X. Zong, M.-L. Fu, S. Chen and L. Wang, *J. Mol. Catal. A*, 2012, **356**, 53.
69 J.-W. Shi, H.-J. Cui, X. Zong, S. Chen, J. Chen, B. Xu, W. Yang, L. Wang and M.-L. Fu, *Appl. Catal. A*, 2012, **435-436**, 86.